The Astrophysical Journal, 596:190–203, 2003 October 10

A *CHANDRA* STUDY OF THE COMPLEX STRUCTURE IN THE CORE OF 2A 0335+096

P. Mazzotta[1] and A. C. Edge
Department of Physics, University of Durham, South Road, Durham DH1 3LE, UK; pasquale.mazzotta@durham.ac.uk

and

M. Markevitch
Harvard-Smithsonian Center for Astrophysics, 60 Garden Street, Cambridge, MA 02138
Received 2003 March 4; accepted 2003 June 19

ABSTRACT

We present a *Chandra* observation of the central ($r < 200$ kpc) region of the cluster of galaxies 2A 0335+096, rich in interesting phenomena. On large scales ($r > 40$ kpc), the X-ray surface brightness is symmetric and slightly elliptical. The cluster has a cool, dense core; the radial temperature gradient varies with position angle. The radial metallicity profile shows a pronounced central drop and an off-center peak. Similarly to many clusters with dense cores, 2A 0335+096 hosts a cold front at $r \approx 40$ kpc south of the center. The gas pressure across the front is discontinuous by a factor $A_P = 1.6 \pm 0.3$, indicating that the cool core is moving with respect to the ambient gas with a Mach number $M \approx 0.75 \pm 0.2$. The central dense region inside the cold front shows an unusual X-ray morphology, which consists of a number of X-ray blobs and/or filaments on scales $\gtrsim 3$ kpc, along with two prominent X-ray cavities. The X-ray blobs are not correlated with either the optical line emission (Hα+[N II]), member galaxies, or radio emission. The deprojected temperature of the dense blobs is consistent with that of the less dense ambient gas, so these gas phases do not appear to be in thermal pressure equilibrium. An interesting possibility is a significant, unseen nonthermal pressure component in the interblob gas, possibly arising from the activity of the central active galactic nucleus (AGN). We discuss two models for the origin of the gas blobs—hydrodynamic instabilities caused by the observed motion of the gas core and "bubbling" of the core caused by multiple outbursts of the central AGN.

Subject headings: cooling flows — galaxies: clusters: general — galaxies: clusters: individual (2A 0335+096) — X-rays: galaxies

1. INTRODUCTION

The cores of clusters contain great dynamical complexity. The presence of gas cooling (Fabian 1994), relativistic plasma ejection from the central galaxy (McNamara et al. 2000; Fabian et al. 2000), the action of magnetic fields (Taylor, Fabian, & Allen 2002), possible thermal conduction (Voigt et al. 2002), local star formation (Allen et al. 1995), and substantial masses of cold ($T < 30$ K) molecular gas (Edge 2001) all complicate the simple hydrostatic picture.

The launch of *Chandra* and *XMM-Newton* has allowed the cores of clusters to be studied in unprecedented detail spatially and spectrally. These advances have led to a number of important results (see, e.g., Peterson et al. 2001; Forman et al. 2002; McNamara 2002). The very restrictive limits on low-temperature gas from *XMM-Newton* Reflection Grating Spectrometer (RGS) spectra are forcing us to reexamine some of the basics paradigms of the cooling flows (see, e.g., Kaastra et al. 2001; Peterson et al. 2001; Tamura et al. 2001; Molendi & Pizzolato 2001). The spatial resolution of *Chandra* can be used to study the brightest nearby cooling flows to advance greatly our understanding of the processes occurring in these regions. In this paper we present the *Chandra* observation of the Zwicky cluster Zw 0335.1+0956, whose properties may help us to address some of the above issues

Zw 0335.1+0956 was first detected as a strong X-ray source by *Ariel 5* (Cooke et al. 1978), and we therefore use the traditional identification 2A 0335+096 in this paper. 2A 0335+096 is among the 25 brightest clusters in the X-ray sky (Edge et al. 1990). The presence of a cooling flow was noted by Schwartz, Schwarz, & Tucker (1980), and its X-ray properties have been studied extensively over the past two decades (Singh, Westergaard, & Schnopper 1986, 1988; White et al. 1991; Sarazin, O'Connell, & McNamara 1992; Irwin & Sarazin 1995; Kikuchi et al. 1999). The optical properties of the central galaxy in 2A 0335+096 have been studied in detail (Romanishin & Hintzen 1988; McNamara, Bregman, & O'Connell 1990), and the strong, extended optical line emission marks this system out as an atypical elliptical galaxy but a prototypical central galaxy in a cooling flow. A deep, multifrequency radio study of 2A 0335+096 (Sarazin, Baum, & O'Dea 1995) shows a weak, flat-spectrum radio source coincident with the dominant galaxy, which is surrounded by an amorphous steep-spectrum "minihalo." The tentative detection of H I absorption (McNamara et al. 1990) and the firm detection of CO emission (implying 2×10^9 $M_\odot$ of molecular gas) and *IRAS* 60 μm continuum (Edge 2001) further highlight this cluster as one for detailed study. The implied mass deposition rate from the CO detection is low (<5 $M_\odot$ yr^{-1}), if the cold molecular gas found is deposited in the cooling flow.

We use $H_0 = 70$ km s^{-1} Mpc^{-1}, $\Omega = 0.3$, and $\Lambda = 0.7$, which imply a linear scale of 0.7 kpc arcsec^{-1} at the distance of 2A 0335+096 ($z = 0.0349$). Unless specified otherwise,

[1] Also, Harvard-Smithsonian Center for Astrophysics, 60 Garden Street, Cambridge, MA 02138.

all the errors are at 90% confidence level for one interesting parameter.

2. DATA PREPARATION

2A 0335+096 was observed on 2000 September 6 with the Advanced CCD Imaging Spectrometer (ACIS), using the back-side–illuminated chip S3. The total exposure time is 21.4 ks. In this paper we concentrate on the bright central $r \lesssim 200$ kpc region of the cluster, which lies fully within the ACIS-S3 chip.

Hot pixels, bad columns, chip node boundaries, and events with grades 1, 5, and 7 were excluded from the analysis. We cleaned the observation of background flares, following the prescription given in Markevitch et al. (2003b). Because chip S3 contains the bright cluster region, we extracted a light curve for the other back-side–illuminated chip S1 in the 2.5–6 keV band, which showed that most of the observation is affected by a mild flare. Because the region of the cluster under study is very bright, we chose a less conservative flare cleaning than is recommended, excluding the time intervals with rates above a factor of 2 of the quiescent rate (taken from the corresponding blank-sky background data set)[2] instead of the nominal factor 1.2. This resulted in the final exposure of 13.8 ks. During the accepted exposure, the front-side–illuminated chips did not exhibit any background rate increases; therefore, the residual background flare is of the "soft" species and can be approximately modeled as described by Markevitch et al. (2003b). We fitted the excess background in chip S1 above 2.5 keV with the flare model and included it, rescaled by the respective solid angle, to the cluster fits. The main component of the background was modeled using the above-mentioned quiescent blank-sky data set, normalized by the rate in the 10–12 keV band (which can be done because the residual flare in our observation is soft and does not affect the high-energy rate). The addition of the flare component has a very small effect on the results, because the cluster core is so bright. The count rates in the S3 chip, energy band 0.3–9.0 keV, from the cluster and the background are 11.8 and 0.39 counts s^{-1}, respectively (at the cluster peak, the cluster count rate is $\approx 10^3$ times higher than the background). We therefore ignored the possible (not yet adequately studied) spatial nonuniformity of the flare component.

3. X-RAY IMAGING ANALYSIS

Figure 1 shows a background-subtracted, vignetting-corrected image of the central region of the cluster, extracted in the 0.3–9 keV energy band and binned to $1''$ pixels. The cluster X-ray surface brightness appears to be regular and slightly elliptical at $r \gtrsim 70''$ (50 kpc). To the south, at about $60''$ (42 kpc) from the X-ray peak, we note the presence of a sharp surface brightness edge similar to those observed in other clusters of galaxies (see, e.g., Markevitch et al. 2000; Vikhlinin, Markevitch, & Murray 2001b; Mazzotta et al. 2001). Finally, the X-ray image shows complex structure in the innermost $\approx 50''$ (35 kpc) region. Below we study these features in detail.

[2] Markevitch (2001); available at http://asc.harvard.edu by choosing successively "Instruments and Calibration," "ACIS," and "ACIS Background."

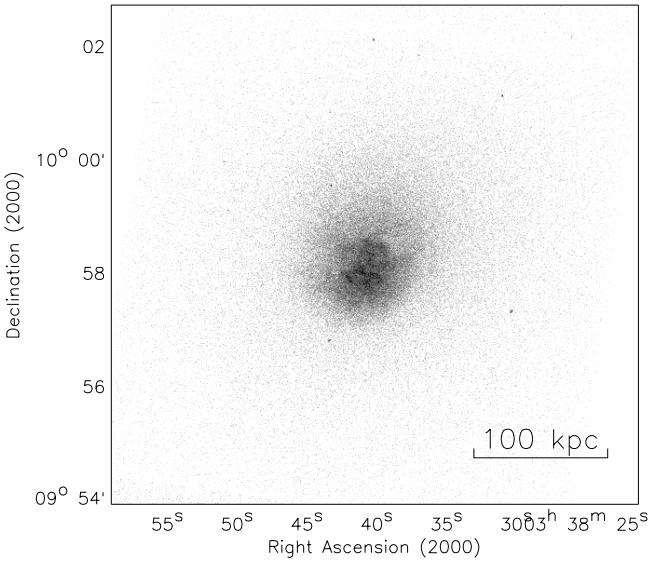

FIG. 1.—Photon image of the central region (ACIS-S3) of 2A 0335+096 in the 0.3–9 keV energy band. The image is background-subtracted, vignetting-corrected, and binned to $1''$ pixels. The image shows a wealth of substructures in the innermost 50 kpc region. Moreover, it shows two significant surface brightness depressions (cavities) on opposite sides of the X-ray peak in the direction northwest-southeast. We also note a surface brightness edge to the south.

3.1. *Core Structure on Larger Scales*

To investigate the cluster spatial structure, and to compare it with previous studies, we start with the classic approach of fitting the surface brightness with a β-model (Cavaliere & Fusco-Femiano 1976). Consistent with previous results, we find that this model does not provide an acceptable fit. Hence, we use a double two-dimensional β-model defined by

$$\Sigma = f_{\rm narrow} + f_{\rm extended} \, . \tag{1}$$

The *narrow* and *extended* components of equation (1) are given by

$$f(r, r_c, \beta, x_0, y_0, \epsilon, \theta) = A\left[1 + \left(\frac{r}{r_c}\right)^2\right]^{-3\beta+1/2} , \tag{2}$$

where

$$r(x, y) = \frac{\sqrt{x_{\rm new}^2(1-\epsilon)^2 + y_{\rm new}^2}}{(1-\epsilon)} , \tag{3}$$

and

$$x_{\rm new} = (x - x_0)\cos\theta + (y - y_0)\sin\theta \, . \tag{4}$$

To perform the fit, we use the SHERPA fitting program.[3] The cluster region with $r > 250''$ and all the strong point sources, together with the regions defined later in § 3.3, are masked out. Because the image contains a large number of pixels with few number counts (<20 counts), we use the Cash (1979) statistics, which, unlike the $\chi 2$ statistics, can be applied regardless of the number of counts per bin. The

[3] See http://asc.harvard.edu; choose the "Data Analysis" menu, then "Introduction."

TABLE 1

RESULT OF FITTING THE CENTRAL 250″ CLUSTER X-RAY IMAGE WITH A DOUBLE TWO-DIMENSIONAL, ELLIPTICAL β-MODEL

Component	Position[a] (J2000.0)	A (counts arcsec^{-2})	r_c (arcsec)	β	ϵ	θ (deg)
Narrow	03 38 40.9, +09 57 57.5	13.2 ± 0.2	85 ± 1	2.45 ± 0.04	0.12 ± 0.008	33 ± 6
Extended	03 38 40.4, +09 58 31.7	5.05 ± 0.06	64 ± 1	0.571 ± 0.004	0.13 ± 0.01	34 ± 4

NOTE.—Units of right ascension are hours, minutes, and seconds, and units of declination are degrees, arcminutes, and arcseconds.

[a] The error of the central position is $\approx 2''$.

best-fit values, with their 90% errors, are reported in Table 1.

Unlike the χ^2 statistics, the magnitude of the Cash statistics depends on the number of bins included in the fit and the values of the data themselves. This means that there is not an easy way to assess from the Cash magnitude how well the model fits the data. To have a qualitative idea of the goodness of the fit, we generate a mock X-ray image using the best-fit values of the double β-model, and we apply the Poisson scatter to it. Consistent with previous studies, we find that globally, the best-fit double β-model describes very well the overall cluster structure. This is evident in Figure 2, where we show the isocontour levels of the model image overlaid on the same isocontour levels of the cluster image after adaptive smoothing. To better illustrate the quality of the fit, we also extract the X-ray surface brightness radial profiles in concentric elliptical annuli from both the cluster and the mock images, as shown in Figure 3. The center, ellipticity, and orientation of each ellipse are set to the best-fit values of the narrow component of the double β-model. The figure clearly confirms the good quality of the fit.

The results of the fit reported in Table 1 show that the two spatial components have very different slopes; in particular, the narrow component is much steeper than the extended one. We also note that the profile of the narrow component derived from the *Chandra* data is significantly steeper than the one obtained from the *ROSAT* PSPC (Kikuchi et al. 1999). The large β-value associated with the narrow component indicates that the cluster contains a very compact and dense gas component with a quite sharp boundary (this is also clearly visible in Fig. 1). On the other hand, the slope of the extended component derived from the *Chandra* data is significantly lower than the value derived from *ROSAT* (see, e.g., Kikuchi et al. 1999; Vikhlinin, Forman, & Jones 1999). Because the *Chandra* result is obtained fitting the cluster surface brightness in a much smaller radial range ($r < 250''$) than the *ROSAT* one ($r \lesssim 1200''$), this indicates that 2A 0335+096 contains one or more radial breaks at $r > 250''$, similar to the ones observed in other clusters, e.g., Hydra A (David et al. 2001) and Perseus (Fabian et al. 2000).

Finally, we note that, although the ellipticity and orientation are similar, the centroid of the two spatial components are offset by $\approx 35''$, with the narrow component centroid being farther south than the extended one.

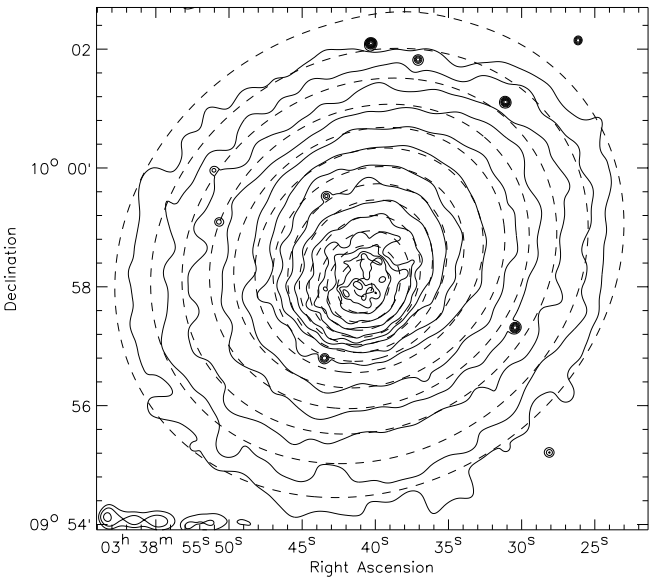

FIG. 2.—Comparison between the X-ray image of 2A 0335+096 and the best-fit double β-model. Solid lines represent isointensity contour levels of the cluster image shown in Fig. 1 after adaptive smoothing. The image was smoothed using a Gaussian kernel with a signal-to-noise ratio (S/N) of the signal under the kernel ≥ 3. The levels are spaced by a factor of $\sqrt{2}$. Dashed lines represent isointensity contour levels of the best-fit double β-model. The levels are the same as for the X-ray image.

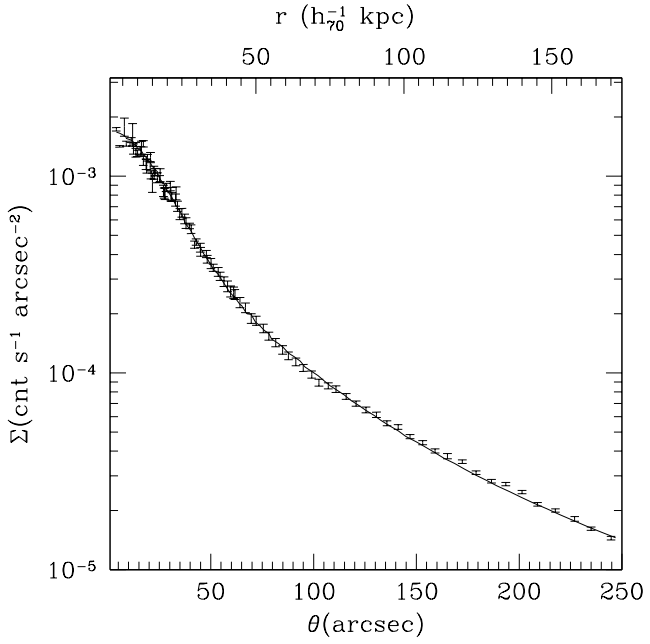

FIG. 3.—Comparison between the surface brightness radial profiles extracted from the X-ray image and the best-fit double β-model. The distance r (as well as Θ) is the geometric mean of the ellipse. To extract the profiles, we used concentric ellipses whose center, ellipticity, and orientation were equal to the best-fit values of the narrow component of the double β-model. Points with error bars and lines correspond to the profiles extracted from the X-ray image and the double β-model, respectively.

Although spatial structure of the cluster is globally well described by a simple double β-model, there are two regions whose structure departs significantly from the best-fit model above: (1) a 60° wide sector to the south and (2) the innermost $r < 50''$ cluster region. Below we study in detail the spatial structure of these regions.

3.2. *X-Ray "Front"*

A closer look at Figure 1 indicates that 2A 0335+096 hosts a surface brightness drop at $r \approx 50''$–$60''$ from the X-ray peak to the south. This X-ray drop spans a sector from 150° to 210° and most closely resembles similar features in other clusters with dense cores and regular morphology on larger linear scales, such as RX J1720+26 and A1795 (Mazzotta et al. 2001; Markevitch, Vikhlinin, & Mazzotta 2001). To better visualize this feature and to study its nature, we extract the cluster X-ray surface brightness profile within the above sector, using elliptical annuli concentric to the brightness edge. The center, ellipticity, and orientation of each ellipse are set to the best-fit values of the narrow component of the double β-model. The profile is shown in the top panel of Figure 4. As extensively shown in previous analysis of cold fronts in clusters of galaxies, the particular shape of the observed surface brightness profile indicates that the density distribution is discontinuous at some radius $r_{\rm jump}$.

To estimate the amplitude and the position of the density jump, we fit the profile using a gas density model consisting of two power laws with index α_1 and α_2 and a jump by a factor A_n at the radius $r_{\rm jump}$:

$$Q = \begin{cases} A_n \left(r/r_{\rm jump}\right)^{\alpha_1} & r < r_{\rm jump} \\ \left(r/r_{\rm jump}\right)^{\alpha_2} & r > r_{\rm jump} \end{cases} . \qquad (5)$$

The fit is restricted to radii $r = 30''$–$200''$, to exclude the central region with irregular structure. We assume spherical symmetry. The best-fit values, together with the 90% confidence level errors, are shown in Table 2. The best-fit model (which provides a good fit to the data) is shown as a solid line in the top panel of Figure 4.

3.3. *Core Structure on Smaller Scales*

To study the cluster morphology on smaller scales, we adaptively smooth the cluster image, as shown in Figure 5. The image was smoothed using the CIAO[4] tool CSMOOTH with a Gaussian kernel and an S/N of the signal under the kernel of ≥ 3.

[4] See http://asc.harvard.edu; choose "Data Analysis."

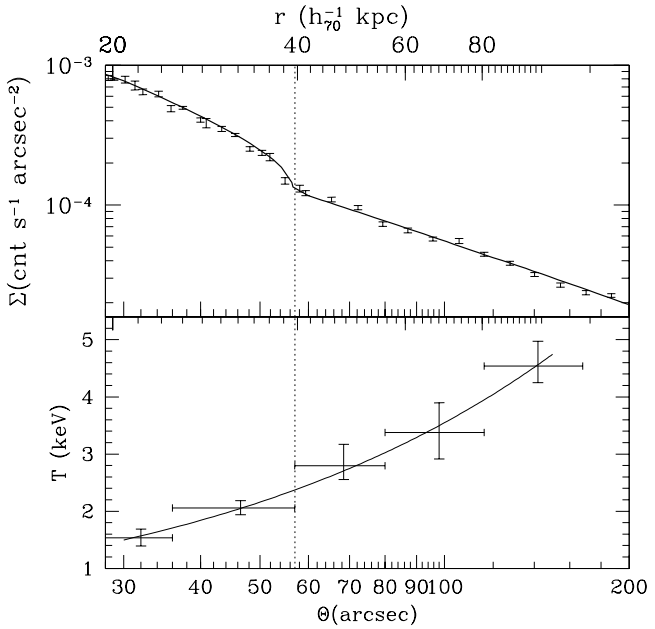

FIG. 4.—*Top*: Cluster surface brightness profile extracted from the 150°–210° sector. The solid line represents the best fit of the discontinuous two–power law density model. *Bottom*: Deprojected temperature profile from the 150°–210° sector. The solid line represents the best fit of the single–power law model.

The image clearly shows a very complex structure, with a number of blobs of X-ray excess emission. The unsmoothed image shows that these blobs are not necessarily distinct but may form a filamentary structure. Nevertheless, for the purpose of our analysis we assume that the X-ray blobs are ellipsoid. We select eight regions, as shown in Figure 5. Each ellipse indicates the region where the surface brightness drops by almost a factor of 2 with respect to the peak of its respective X-ray blob. One of the largest uncertainties in the estimate of the blob densities is connected with the unknown projected distance of each blob and hence their actual volume. In order to obtain an estimate of the density, we make the simple assumption that the radius r_3 of the ellipsoid along the line of sight is the mean value of the major radius r_1 and minor radius r_2. As error for r_3 we assume the difference between r_2 and r_1. In Table 3, we report the major and the minor radii corresponding to each region shown in Figure 5. The dimensions of the X-ray blobs span from 4″ to 9″ (from 2.8 to 6.3 kpc). We calculate the mean electron density using the following procedure. Using the method described in § 4, we extract the spectra from both the blob region and a cluster region just outside it. Using the latter spectrum as background, we fit the blob

TABLE 2

X-RAY FRONT DENSITY, TEMPERATURE, AND PRESSURE BEST-FIT VALUES

Quantity	α_1	α_2	A_n	$r_{\rm jump}$ (arcsec)
Density (n)	-1.36 ± 0.04	-1.20 ± 0.02	1.6 ± 0.02	56.7 ± 1
Temperature (T)	$+0.79 \pm 0.03$	$+0.67 \pm 0.20$	1.0 ± 0.20	...
Pressure (P)	-0.57 ± 0.05	-0.53 ± 0.20	1.6 ± 0.30	...

NOTES.—Each quantity is modeled using two power laws with a jump (eq. [5]). Errors are 90% confidence level.

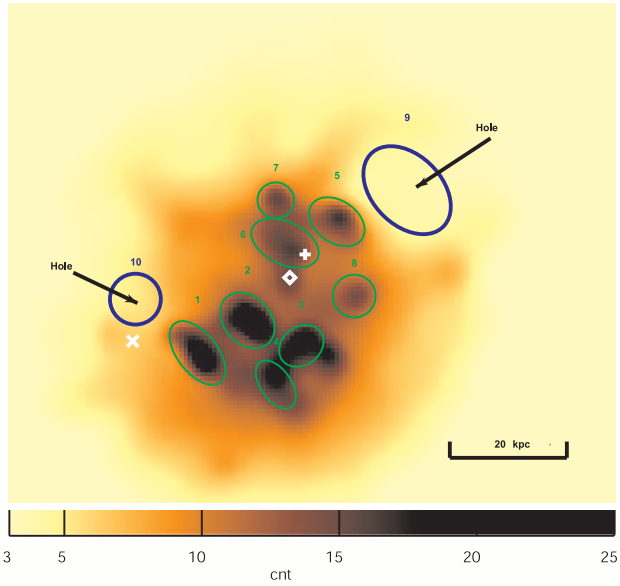

FIG. 5.—Zoom-in of Fig. 1 after adaptive smoothing made using a Gaussian kernel with an S/N of the signal under the kernel ≥ 3. The green ellipses labeled from 1 to 8 identify eight X-ray–bright extended regions, or blobs. The two blue ellipses, labeled 9 and 10, identify the western and eastern X-ray holes, or cavities. The diamond and plus sign indicate the positions of the cluster D galaxy and its companion, respectively. The cross indicates the position of the other cluster central galaxy (see Fig. 10).

spectrum with a thermal model, hence deriving the emission measure. Finally, the gas density is calculated from the emission measure, under the simple assumption that it is constant within the blob. The net number of counts and the mean gas densities obtained using the above procedure are reported in Table 3. By comparing the number counts in each blob region with the ones in a region just outside it and assuming Poissonian statistics, we find that all the observed blobs are highly statistically significant ($\geq 6\ \sigma$ confidence level; see col. [5] in Table 3).

Beside the X-ray blobs, we also note two X-ray holes: at 30″ (21 kpc) to the northwest and ≈40″ (38 kpc) to the east of the X-ray peak. To check the statistical significance of the holes, we extract the count rates from elliptical regions in each hole (see Fig. 5) and the count rates in two similar regions to the east and west of the depressions along the isocontour level defined by the best-fit double β-model. The absorbed flux from both holes is ≈20% lower than the flux from the neighboring regions, at a 4.5 and 7.5 σ confidence level for the eastern and northwestern holes, respectively. As shown in § 5, the cluster image may also present other X-ray holes at larger radii. The previous identification of the eastern hole from *ROSAT* HRI observations with absorption by a cluster member galaxy, by Sarazin et al. (1992, 1995), is not supported by these higher resolution images (see Fig. 5).

4. SPECTRAL ANALYSIS

We use the CIAO software to extract spectra. The spectra are grouped to have a minimum of 20 net counts per bin and fitted using the XSPEC package (Arnaud 1996). The position-dependent RMFs and ARFs are computed and weighted by the X-ray brightness over the corresponding image region using the *calcrmf* and *calcarf* tools.[5] To account for the absorption caused by molecular contamination of the ACIS optical blocking filters,[6] all the spectral models we use are multiplied by the ACISABS absorption model[7] that models the above absorption as a function of time since launch. The parameter TDAYS is set to 410, while the others are left at the default values, namely, NORM = 7.22×10^{-3}, TAUINF = 0.582, TEFOLD = 620, NC = 10, NH = 20, NO = 2, and NN = 1.

Spectra are extracted in the 0.6–9.0 keV band in PI channels. At present, the ACIS response is poorly calibrated around the mirror Ir edge, which results in frequently observed significant residuals in the 1.4–2.2 keV energy interval and high χ^2 values. We tried excluding this energy interval and found that the best-fit parameter values and confidence intervals do not change considerably, while the χ^2 values become acceptable, as is seen below. We therefore elected to use the full spectral range.

4.1. *Average Temperature*

To determine the average spectral properties of this observation, we extract the overall spectrum from the inner-

[5] A. Vikhlinin (2000); available at http://asc.harvard.edu by choosing the link "Contributed Software Exchange."

[6] See http://asc.harvard.edu, choosing in succession "Instruments and Calibration," "ACIS," and "ACIS EQ Degradation.".

[7] Chartas & Getman (2002), available at http://www.astro.psu.edu/users/chartas/xcontdir/xcont.html.

TABLE 3
SPATIAL AND SPECTRAL PROPERTIES OF THE X-RAY BLOBS

Region (1)	r_1 (arcsec) (2)	r_2 (arcsec) (3)	Net Counts (0.6–9 keV) (4)	Confidence Level (σ) (5)	n_e ($\times 10^{-2}$ cm^{-3}) (6)	T (keV) (7)	$T_{\rm depr}$ (keV) (8)	$L_{0.6-9}$ ($\times 10^{41}$ ergs s^{-1}) (9)	τ_c ($\times 10^8$ yr) (10)
1	9.0	4.8	796	14.5	7.7 ± 1	1.41 ± 0.04	$1.17^{+0.13}_{-0.12}$	5.8	2.0 ± 0.3
2	7.5	5.6	1092	19.2	9.4 ± 0.7	$1.40^{+0.03}_{-0.04}$	$1.22^{+0.10}_{-0.14}$	8.2	1.9 ± 0.2
3	5.8	4.6	724	14.2	12.0 ± 0.7	$1.73^{+0.08}_{-0.09}$	$1.64^{+0.18}_{-0.20}$	6.4	2.1 ± 0.3
4	6.6	3.7	582	11.5	11.0 ± 1	1.55 ± 0.10	$1.40^{+0.18}_{-0.12}$	4.6	2.4 ± 0.4
5	7.4	5.1	405	8.5	5.9 ± 0.5	$1.76^{+0.17}_{-0.09}$	$1.00^{+0.29}_{-0.20}$	2.7	2.4 ± 0.8
6	8.7	5.1	684	12.7	8.7 ± 1	1.95 ± 0.14	$2.02^{+0.51}_{-0.30}$	7.5	4.1 ± 1.2
7	4.4	4.3	223	6.4	8.2 ± 0.2	$1.79^{+0.31}_{-0.12}$	$1.67^{+0.86}_{-0.36}$	1.8	3.3 ± 2.0
8	5.2	5.2	312	7.5	7.2 ± 0.2	$1.63^{+0.10}_{-0.11}$	$1.28^{+0.24}_{-0.25}$	2.4	2.8 ± 0.6

TABLE 4
COMPARISON OF SPECTRAL FITS FOR THE INNERMOST 250″ REGION

Model	N_H ($\times 10^{21}$ cm^{-2})	T_1 (keV)	T_2 (keV)	$Z/Z_\odot$	$\dot{M}$ ($M_\odot$ yr^{-1})	χ^2/dof
TBABS×MEKAL	1.6	2.7	...	0.59	...	843/352
	(1.6 ± 0.02)	(2.6 ± 0.05)	...	(0.54 ± 0.04)	...	(484/297)
TBABS×[MEKAL+MEKAL]	$1.71^{+0.06}_{-0.05}$	$3.3^{+0.9}_{-0.2}$	$1.4^{+0.3}_{-0.1}$	0.55 ± 0.05	...	643/350
	$(1.71^{+0.08}_{-0.07})$	$(3.0^{+0.9}_{-0.2})$	$(1.4^{+0.3}_{-0.2})$	(0.53 ± 0.06)	...	(393/295)
TBABS×[MEKAL+MKCFLOW]	2.0 ± 0.1	2.90 ± 0.1	...	0.68 ± 0.04	247^{+37}_{-34}	658/351
	(2.0 ± 0.1)	(2.78 ± 0.06)	...	(0.60 ± 0.04)	(192^{+37}_{-34})	(387/296)
TBABS×[MEKAL	0.9 ± 0.2[a]	3.0 ± 0.1	...	0.68 ± 0.02	266^{+35}_{-36}	658/351
TBABS×[MEKAL+ZTBABS(MKCFLOW)]	(1.3 ± 0.4)[a]	(2.8 ± 0.1)	...	$(0.61^{+0.05}_{-0.04})$	(249^{+65}_{-60})	(393/296)

NOTE.—Values in parentheses are from fits with the excluded 1.4–2.2 keV energy interval.
[a] Intrinsic absorption.

most circular region of $r = 250''$ (175 kpc) centered on the X-ray peak and fit it with different models, as listed in Table 4. In the following, the absorption of X-rays due to the interstellar medium has been parameterized using the Tübingen-Boulder model (TBABS in XSPEC, ver. 11.1; Wilms, Allen, & McCray 2000). Furthermore, the metallicity refers to the solar photospheric values in Anders & Grevesse (1989). As a first attempt, we use an absorbed, single-temperature thermal model (TBABS × MEKAL; see, e.g., Kaastra 1992, Liedahl, Osterheld, & Goldstein 1995, and references therein). We find that this model does not reproduce the spectrum. We also use an absorbed, two-temperature model (TBABS × [MEKAL + MEKAL]), with the metallicity of the two components linked together. The hydrogen equivalent column density and the temperature, metallicity, and normalization of each thermal component are left free to vary. This model provides a much better fit. In particular, if we exclude the energy band near the Ir edge from the spectral analysis, we find that the model is statistically acceptable (see Table 4). We find that the equivalent column density is consistent with the Galactic value ($N_H = 1.78 \times 10^{21}$ cm^{-2}; Dickey & Lockman 1990). The temperatures of both the hot and the cool components, as well as the metallicity, are consistent with the values obtained from the combined analysis of *ASCA* GIS and SIS spectra extracted from the innermost $r = 120''$ region (Kikuchi et al. 1999). We finally fit the spectrum using two models with cooling flows. The first is an absorbed thermal model plus a cooling flow component (TBABS × [MEKAL + MKCFLOW]). In the second, we assume that the cooling flow component itself is intrinsically absorbed by uniformly distributed amount of hydrogen at the cluster redshift (TBABS × [MEKAL + ZTBABS(MKCFLOW)]), in XSPEC, ver. 11.1). The higher temperature and metallicity of the cooling flow component are fixed to be equal to those of the thermal component. In the first cooling flow, we leave the absorption free to vary. In the intrinsically absorbed cooling flow model, we fix the overall absorption to the Galactic value and leave the intrinsic N_H free to vary. We find that both models give temperatures, metallicities, and the mass deposition rates consistent within the errors. It is worth noting that the cooling flow models give a minimum χ^2 value similar to that of the two-temperature model, which, as noted above, is quite high compared to the degrees of freedom (dof).

4.2. *Temperature Map*

To determine the temperature map, we used the same technique used for A3667 (Vikhlinin et al. 2001b; Mazzotta, Fusco-Femiano, & Vikhlinin 2002). We extracted images in 10 energy bands, 0.80–1.07–1.43–1.68–1.82–2.16–2.35–2.88–3.75–5.83–9.00 keV, subtracted background, masked out point sources, divided by the vignetting maps, and smoothed the final images. We determined the temperature by fitting the 10 energy points to a single-temperature absorbed MEKAL plasma model with metal element abundance fixed at $Z = 0.6\ Z_\odot$. We left as free parameters the equivalent absorption column density, the temperature, and the normalization.

To study the cluster temperature structure at larger radii (where the cluster is less bright), we derive first a relatively low spatial resolution temperature map. This is obtained by smoothing the 10 images above using a Gaussian filter with $\sigma = 15''$. The "low-resolution" temperature map, overlaid on the 0.3–9 keV ACIS brightness contours, is shown in the left-hand panel of Figure 6. Like the surface brightness, the projected temperature map is not azimuthally symmetric. The gas is substantially cooler in the cluster center and shows a strong positive temperature gradient that varies with position angle. The temperature gradient seems to be higher and lower in the southern and northern sectors, respectively. It is interesting to note that the gradient seems to be at maximum somewhere in the southern sector, where we observe the surface brightness edge.

To study the thermal properties of the X-ray blobs and cavities discussed in § 3.3, we produce a second temperature map of the innermost central region, using a much higher spatial resolution. This region is identified by the green ellipse in the left-hand panel of Figure 6. The "high-resolution" temperature map, overlaid on the 0.3–9 keV ACIS brightness contours, is shown in the right-hand panel of Figure 6. The map is obtained by smoothing the 10 images above using a very narrow Gaussian filter with $\sigma = 4''$. For clarity, we plot ellipses numbered from 1 to 10, corresponding to the eight X-ray blobs and two cavities defined in § 3.3 (see also Fig. 5). The high-resolution temperature map shows a very complex structure. In particular, the cavities and the X-ray blobs seem to have quite different projected temperatures. We discuss this aspect in § 4.5.

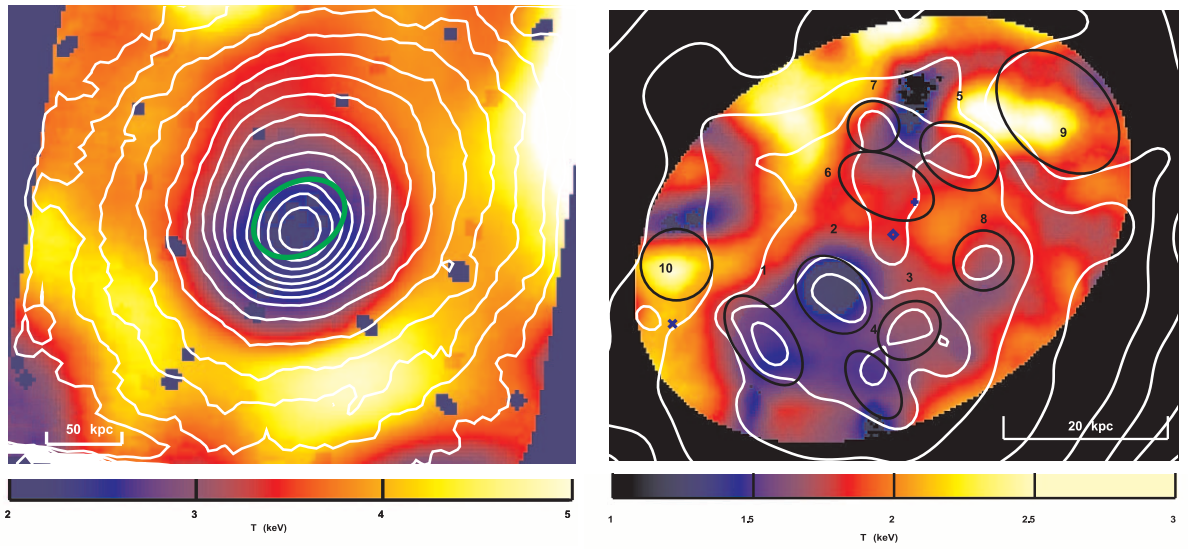

FIG. 6.—Temperature map of 2A 0335+096 overlaid on the 0.3–9 keV ACIS brightness contours. *Left*: This temperature map was obtained by smoothing the images using a Gaussian filter with $\sigma = 15''$. The green ellipse corresponds to the temperature map in the right-hand panel. Blue holes indicate the positions of the point sources that were masked out. The isocontours are obtained from the image after a Gaussian smoothing with $\sigma = 15''$. Levels are spaced by a factor of $\sqrt{2}$. *Right*: Zoom-in, high-resolution temperature map from the cluster inside the green ellipse in the left-hand panel. This temperature map was obtained by smoothing the images using a Gaussian filter with $\sigma = 4''$. Isolevels are the same as in the solid lines in Fig. 2. The ellipses labeled from 1 to 10 identify the regions defined in Fig. 5. The blue diamond, plus sign, and cross indicate the position of the galaxies as in Fig. 5.

4.3. *Radial Temperature Gradients*

We first measure the overall spectral radial properties by extracting spectra in concentric elliptical annuli. The center, ellipticity, and orientation of each ellipse are fixed to the best-fit values of the narrow component of the double β-model, as shown in Figure 3. The radii are chosen in order to have ≈20,000 net counts per spatial bin. Each spectrum is fitted with an absorbed, one-temperature MEKAL model. Equivalent hydrogen column density, temperature, metallicity, and normalization are left free to vary. We get an acceptable fit for all the annuli but the innermost one. The resulting temperature, metallicity, and $N_{\rm H}$ profiles, with error bars at the 1 σ level, are shown in the top, middle, and bottom panels of Figure 7, respectively (errors bars are at the 1 σ level). The temperature profile shows a positive gradient within the innermost 50–60 h_{70}^{-1} kpc, with a temperature that goes from ≈1.5 to ≈3.5 keV. At larger radii the temperature profile shows a much flatter profile, consistent with being constant. Only the last bin, at 150 h_{70}^{-1} kpc, indicates a possible temperature increment at larger radii. Although the cluster is clearly not spherically symmetric, we try to deproject the overall temperature profiles assuming that it actually is. To deproject the temperature profile, we use the simple technique described by Allen, Ettori, & Fabian (2001). For the deprojected temperature profile, we get an acceptable fit for all the annuli, including the innermost one. The deprojected profile is plotted as dotted crosses in the top panel of Figure 7. We note that the deprojected temperature of the innermost bin is $T = 1.36 \pm 0.02$ keV.

The projected metallicity is consistent with the constant value $Z \approx 0.5\ Z_{\odot}$ at radii greater than 50–60 h_{70}^{-1} kpc. At lower radii it shows a strong positive gradient, with a maximum of ≈0.8 $Z_{\odot}$ at 40 h_{70}^{-1} kpc. Similar metallicity gradients have been observed in other clusters, e.g., M87 (Molendi & Gastaldello 2001), Perseus (Schmidt, Fabian, & Sanders 2002), A2052 (Blanton, Sarazin, & McNamara 2003), A2199 (Johnstone et al. 2002), and Centaurus (Sanders & Fabian 2002). For some of them, however, it has been shown that the gradient is an artifact induced by the inadequate modeling of the spectra with a single-temperature

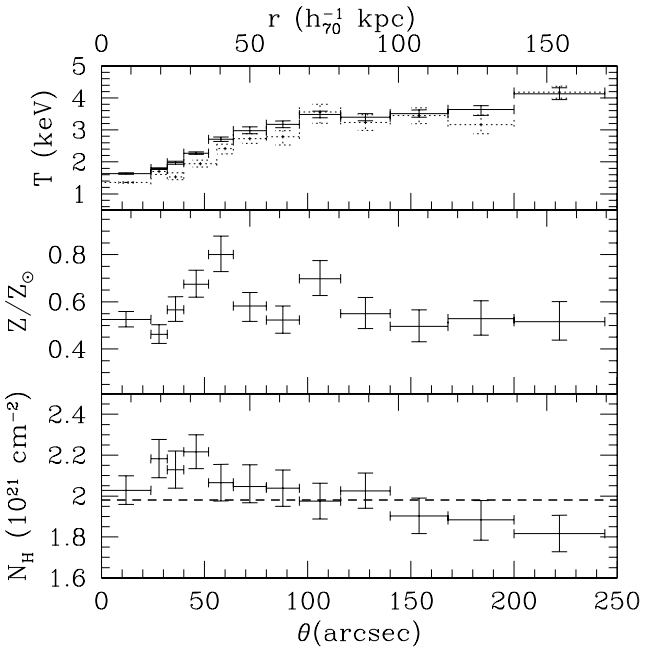

FIG. 7.—Emission-weighted temperature, metallicity, and equivalent column density radial profiles of 2A 0335+096. The spectra are extracted in concentric elliptical annuli. The center, ellipticity, and orientation of each ellipse are fixed to the best-fit values of the narrow component of the double β-model, as shown in Fig. 3. The distance r (as well as Θ) is the geometric mean of the ellipse. The dotted crosses in the top panel indicate the results obtained by deprojecting the temperature profiles on the assumption of spherical symmetry. The dotted line in the bottom panel is $N_{\rm H}$ value obtained by fitting a constant to the $N_{\rm H}$ profile. Error bars are 1 σ confidence level.

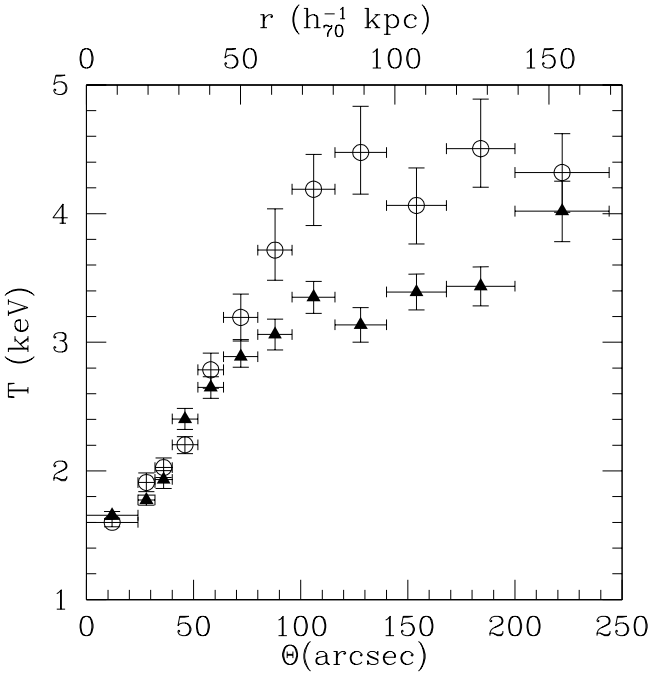

FIG. 8.—Comparison of the temperature profiles extracted from the northern (*triangles*) and southern (*circles*) halves of the cluster.

component where a multitemperature one is actually required. This effect is known as metallicity bias (see Buote 2000). It is interesting to note, however, that if we deproject the metallicity profile assuming spherical symmetry, we find that the profile is consistent with the projected one. This indicates either that the spherical symmetry assumption is inadequate or that the gradient is real. Recently, Morris & Fabian (2003) suggested that apparent off-center peaked metallicity profiles may form as a result of the thermal evolution of intracluster medium with a nonuniform metal distribution.

Finally, as shown in the bottom panel of Figure 7, we find that the equivalent column density profile is consistent with a constant value of 1.98×10^{21} cm^{-2}, which seems to be 10% higher than the Galactic value.

As discussed in § 4.2, the cluster temperature distribution is strongly asymmetric. To verify the statistical significance of this asymmetry, we extract the spectra using the photons from the northern or the southern sector. Spectra are extracted in the elliptical annuli, with the same binning as before. We find that, although both the $N_{\rm H}$ and metallicity profiles from the northern and the southern sectors are consistent within the errors, the temperatures profiles are significantly different. Figure 8 clearly shows that the temperature gradient in the northern sector is shallower than the gradient in the southern sector. Moreover, the region of constant temperature in the southern sector is a factor of 1.3 hotter than that in the northern sector.

4.4. *Temperature Profile of the Front*

In § 3.2, we show that the cluster has a surface brightness edge similar to the cold fronts observed in other clusters of galaxies. One peculiar characteristic of these cold fronts is that they have a temperature discontinuity (jump) over the front itself. In this paragraph, we study the thermal properties of the X-ray front in 2A 0335+096. To do this, we estimate the three-dimensional temperature profile of the front by deprojecting the temperature profile from the cluster sector whose angles are from 150° to 210°. The three-dimensional temperature profile is shown in the bottom panel of Figure 4. We note that the temperature profile has a quite steep gradient. Moreover, unlike the cold fronts observed in other clusters of galaxies, it does not show a clear temperature discontinuity at the front. At first, we fit the temperature profile in the range from 30″ to 150″ with a single–power law model, $T \propto \theta^{\delta}$. The model provides a good fit, with $\delta = 0.72 \pm 0.02$, as shown in Figure 4. We note that the data may also be consistent with a small temperature jump at the front. To constrain the amplitude of this possible jump, we fit the data using a two–power law model with a jump A_T at the position of the front (see eq. [5]), and we report the result in Table 2. From the table we see that $A_T = 1 \pm 0.2$. Using the pressure and the density models above, we calculate the pressure profile near the front region. The best-fit model, together with the 90% errors, is reported in Table 2. The observed density and temperature discontinuity at the front result in corresponding pressure discontinuity of a factor $A_P = 1.6 \pm 0.3$.

4.5. *Spectral Properties of the X-Ray Blobs and Cavities*

As discussed in § 4.2, the innermost region of 2A 0335+096 has a very complex temperature structure. In particular, the temperature map shows that the cavities and the X-ray blobs have quite different projected temperatures (see Fig. 6). To better study the thermal properties of these structures, we extract spectra for all the elliptical regions shown in the figure and fit them with an absorbed thermal model. We verify if there is any excess absorption by fixing the metallicity to $Z = 0.6$ solar and letting both $N_{\rm H}$ and the temperature vary freely. As we find that the resulting $N_{\rm H}$ values are all consistent with the cluster mean value, we fix $N_{\rm H}$ to this value and refit the model to measure the temperature. The projected temperatures of the blobs, together with the 90% error bars, are reported in Table 3 and shown as squares in Figure 9. Consistent with the right-hand panel of Figure 6, we find that the central X-ray structures have different projected temperatures. In particular, we note that regions 1 and 2 are significantly cooler than regions 6 and 7. Furthermore, we note that the holes are significantly hotter than any of the X-ray blobs, as their temperatures are $T = 2.5 \pm 0.3$ and 2.5 ± 0.5 keV for the western and eastern holes, respectively. It is worth noting that the observed higher temperature in the holes is likely to be the result of a projection effect.

Projection could also be responsible for the observed difference in the projected temperature of the X-ray blobs. To verify this hypothesis, one should find a way to disentangle the contribution to the spectrum due to the blob itself from that due to the gas along the line of sight. To perform this task, we assume that the contribution to the spectra due to the gas along the line of sight is almost the same within the innermost 25″ region (where all the blobs are). This is justified by the fact that, if we exclude the blobs, the surface brightness profile within this region does not vary by more than a factor of ≈1.5. We then extract a cluster spectrum, using a region just outside the blobs that will be used as background for the spectrum of each blob. The first important result of this exercise is that the final spectrum clearly shows the presence of Fe L emission-line complex. This

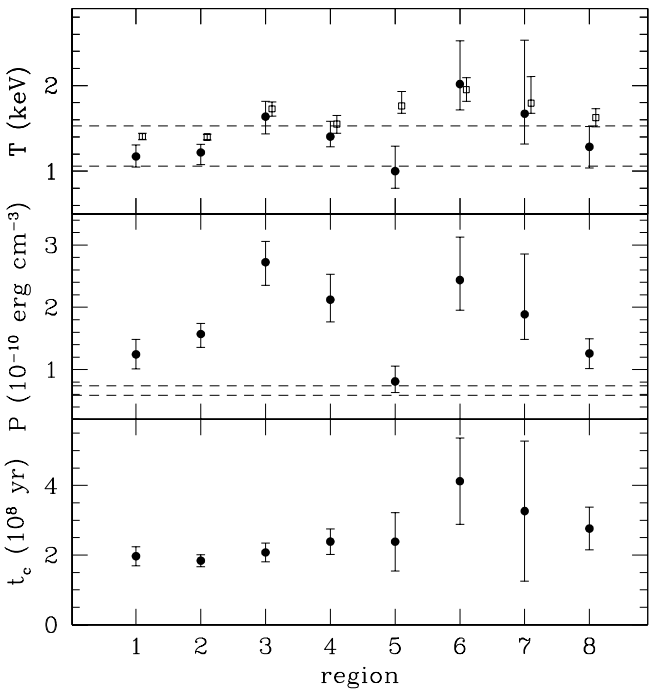

FIG. 9.—*Top*: Temperature associated with each of the X-ray blob regions defined in Fig. 5. Squares show the projected temperatures of the blobs, while circles indicate the temperatures after deprojection (see text). The dashed lines represent the 90% confidence level error measurement on the deprojected temperature of the ambient gas. *Middle*: Thermal pressure associated with the same blobs as in the top panel. The dashed lines represent the 90% confidence level error measurement of the thermal pressure of the ambient gas. *Bottom*: Cooling time associated with the same blobs as in the top panel.

proves, without doubt, that the emission from these blobs is indeed mostly, if not all, thermal. We fit these spectra using a single-temperature MEKAL model, leaving as free parameters only the temperature and the normalization. The result is shown in the top panel of Figure 9. In the same figure we add, as dashed lines, the 90% error temperature estimate of the ambient gas. This estimate comes from the fit of the blob-free cluster spectrum, used above as background, with a two-temperature MEKAL model with the metallicity of the two thermal components linked together. To compensate for our ignorance of the actual three-dimensional cluster structure, we leave the normalizations of both thermal components free to vary. We assume that the temperature of the ambient gas coincides with that of the lower temperature component. We believe that this represents a fair assumption. We note that this temperature is consistent with the temperature of the innermost bin obtained with the independent approach of the spherical symmetric deprojection model (see top panel of Fig. 7).

Notably, all regions but the sixth have temperatures consistent with the three-dimensional temperature of the ambient gas. Using the blob density measurements reported in Table 3, it is now possible to estimate the thermal pressure associated with each blob. This is shown in the middle panel of Figure 9. In the same figure we plot as dashed lines the 90% error ambient pressure. The blobs, except region 5, have thermal pressure values significantly higher than the ambient thermal pressure. This unexpected finding is discussed below.

Using the temperature and density of each blob, we also estimate their cooling times $\tau_c \equiv 5P/2\epsilon$, where P and ϵ are the blob's pressure and the emissivity, respectively. These, together with the 90% error bar, are shown in the bottom panel of Figure 9. We note that all blobs have similar cooling times, which are consistent within the errors (but see region 6). For practical reasons, we report also the blob cooling times in column (10) of Table 3.

For completeness, we estimate the X-ray blob unabsorbed luminosities in the (0.6–9.0) keV in the source rest frame, as shown in column (9) of Table 3.

5. PROPERTIES AT OTHER WAVELENGTHS

We conclude the analysis of 2A 0335+096 by comparing the cluster properties in the X-rays to those at other wavelengths.

In Figure 10, we show a *Hubble Space Telescope* (*HST*) image of the central region of 2A 0335+096, superposed on contours of the X-ray image after adaptive smoothing. The optical image shows one central D galaxy (PGC 013424; Paturel et al. 1989), with a companion smaller galaxy 7″ to the northwest and another elliptical galaxy at 41″ to the east. In Figure 10, the X-ray blobs defined in § 3.3 (labeled 1–8 in Fig. 5) can be easily identified by matching the small, quasi-elliptical isocontour regions. Apart from one X-ray blob coincident with the cluster D galaxy, none of the other blobs have optical counterparts. This strongly suggests that the X-ray blobs are produced by some kind of hydrodynamic process.

For completeness, in Figure 10 we report the centroid position of the narrow and extended β-model components. It is worth noting that the D galaxy position does not coincide with either of these centroids, but rather lies in between.

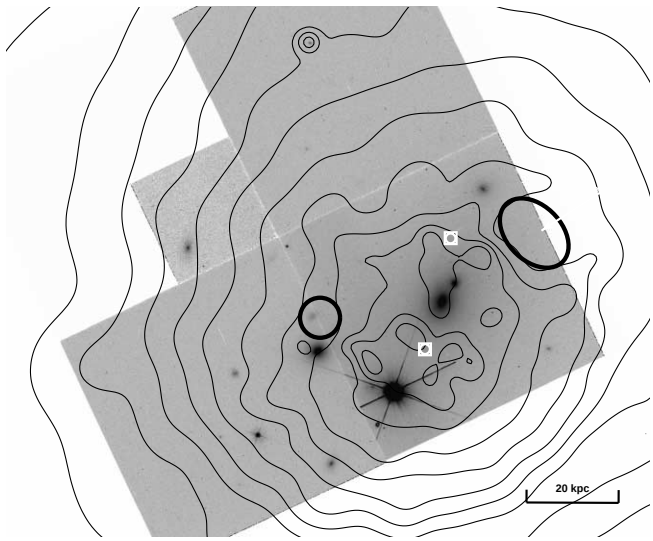

FIG. 10.—*HST* image of the central region of 2A 0335+096, superposed on contours of the X-ray image after adaptive smoothing. The circle-in-square symbols indicate the best-fit central position of each of the components of the double β-model. The northern and southern symbols indicate the positions of the extended and narrow components, respectively. The thick ellipses indicate the positions of the western and eastern holes. The X-ray excess regions labeled 1–8 in Fig. 5 can be easily identified by the small quasi-elliptical isocontour regions. Note that none of these regions has an optical counterpart.

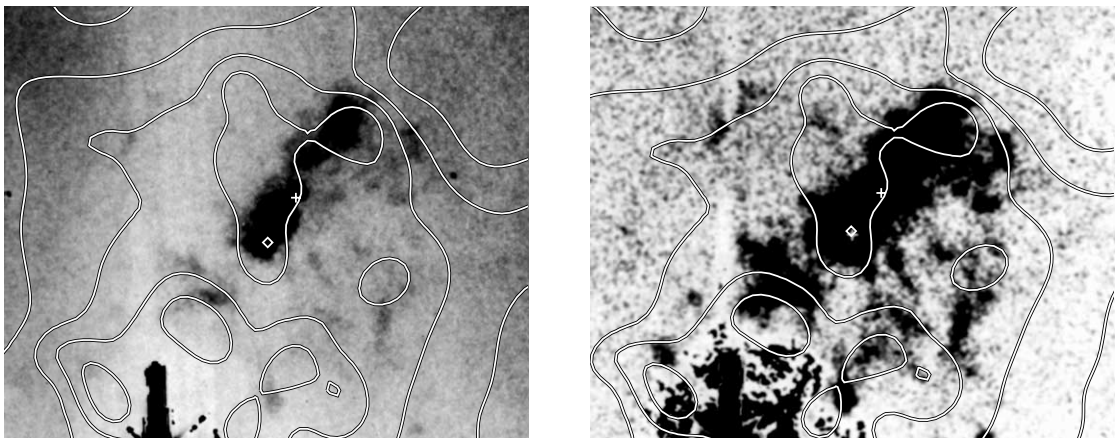

FIG. 11.—Hα+[N II] image of the central $60'' \times 70''$ region of 2A 0335+096 (from Romanishin & Hintzen 1988, their Fig. 3), with X-ray contours overlaid. The X-ray contours are the same as in Fig. 10. To better visualize the faintest line features, we show the Hα+[N II] image in both high (*left*) and low (*right*) contrast. The diamond and the plus sign indicate the position of the central D galaxy and its companion, respectively. The X-ray excess regions labeled 1–8 in Fig. 5 can be easily identified by the small quasi-elliptical isocontour regions. The western X-ray cavity is located in the upper right-hand corner. Note that the large, bright artifact in the lower left of the image is a saturated star.

The central galaxy of 2A 0335+096 has been found to have a number of peculiar properties over the past two decades. Initially, it was classified as a Seyfert 1.5 galaxy or LINER by Huchra, Wyatt, & Davis (1982), but more detailed optical observations by Romanishin & Hintzen (1988) found a very extended optical emission line region (Hα+[N II]) to the northeast of the galaxy (extended over 30 kpc), and the central regions of the galaxy are anomalously blue, indicating recent star formation (see Fig. 11). Recently, a number of authors have shown that some of the extended Hα features observed in the central region of a number of clusters correlate with similar structures of X-ray excess (e.g., A1795: Fabian et al. 2001; RX J0820.9+0752: Bayer-Kim et al. 2002; Virgo: Young, Wilson, & Mundell 2002).

To study the correlation between the X-ray blobs and the line emission in Figure 11, we show the narrowband Hα+[NII] image from Romanishin & Hintzen (1988), with the X-ray isocontours superposed. The accuracy of the alignment is better than $3''$. There is no direct correlation between the X-ray and Hα+[N II] structures, but there is a tendency for the two to lie close to each other. However, the statistical significance of this tendency is difficult to judge. Note that the X-ray blobs labeled 1 and 4 lie too close to the saturated star to the southeast of the Hα+[N II] image to detect the fainter Hα+[N II] emission.

The radio properties of 2A 0335+096 are also of note. Sarazin et al. (1995) find an amorphous, steep-spectrum ($\alpha \sim -1.4$) minihalo around PGC 013424, which has relatively low radio power compared to other similar systems. Figure 12 shows the image of the percentile variation $[(\Sigma_{\rm cl} - \Sigma_{\rm mod})/\Sigma_{\rm cl}]$ of the cluster X-ray surface brightness $\Sigma_{\rm cl}$ with respect to the best-fit double β-model $\Sigma_{\rm mod}$. The isocontours of the VLA[8] 1.5 GHz C+D configuration image (resolution $16''$) from Sarazin et al. (1995) are superposed. The image clearly shows the position of the X-ray front, together with the X-ray blobs and the western and eastern holes studied in §§ 3.2 and 3.3, respectively. We note that the mini–radio halo is well within the radius defined by the position of the X-ray front. Unfortunately, the spatial resolution of the radio map is insufficient to correlate it with the X-ray blobs. However, there is some indication that, as observed in other clusters (see McNamara 2002 for a review), both X-ray holes contain some steep-spectrum radio emission (D. Harris 2003, private communication) which may be "relic" emission from previous radio lobes.

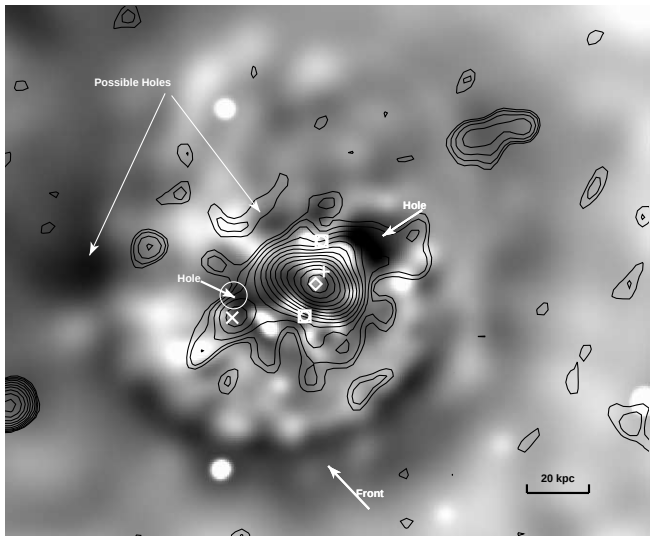

FIG. 12.—Percentile variation of the cluster X-ray image (after adaptive smoothing) with respect to the best-fit double β-model, superposed on contours of the 1.515 GHz radio image (from Sarazin et al. 1995). Isocontour levels correspond to (0.15, 0.20, 0.35, 0.60, 0.95, 1.40, 1.95, 2.60, 3.40, 4.20, 5.20, 6.20, 7.40, 8.60, 10) mJy beam^{-1}, with a beam size of FWHM $12''.8 \times 12''.4$. The darker and lighter regions indicate negative and positive variation of $\geq |20|\%$, respectively. The arrows indicate the position of the western and eastern holes and the position of the front. The diamond and plus sign indicate the position of the central D galaxy and its companion, respectively, while the cross indicates the position of the third cluster galaxy in the *HST* field (see Fig. 10). Finally, the circle-in-square symbols indicate the best-fit central position of each of the components of the double β-model.

[8] The VLA (Very Large Array) is a facility of the National Radio Astronomy Observatory (NRAO). The NRAO is a facility of the National Science Foundation operated under cooperative agreement by Associated Universities, Inc.

Future high-resolution, low-frequency radio observations will be crucial to linking the mini–radio halo and X-ray structure.

It is worth noting that Figure 12 also suggests the presence in 2A 0335+096 of ghost X-ray bubbles at larger radii, similar to the ones observed in other clusters (McNamara 2002). Unfortunately, because of the relatively short exposure, these bubbles are not statistically significant. A deeper X-ray observation is needed to confirm their existence.

6. DISCUSSION

The *Chandra* observation of 2A 0335+096 reveals that the core region of this otherwise relaxed cluster is very dynamic.

The cluster image shows an edgelike feature at 40–90 kpc from the X-ray peak to the south. The edge spans a sector from 150° to 210° from the north. On smaller scales (<20 kpc), the cluster image shows a very complex structure, with X-ray filaments or blobs. Moreover, it shows the presence of two X-ray cavities (see Fig. 5).

The spectral analysis clearly shows that on large scales the cluster temperature distribution is not azimuthally symmetric (see §§ 4.2 and 4.3). Furthermore, the cluster gas temperature reaches its maximum in a region at ≈90 kpc from the X-ray peak to the south, just beyond the surface brightness edge (Fig. 6). On smaller scales, the X-ray blobs have similar temperatures but different pressures.

Below we discuss the results of our analysis and propose possible dynamical models that may explain the observed properties of the core of 2A 0335+096.

6.1. *Nature of the Surface Brightness Edge: A Cold Front*

In § 3.2, we analyze the spatial structure of the X-ray front. We show that the front is well fitted by a discontinuous density profile, with a density jump at the front of a factor of ≈1.6. Similar density jumps have been observed by *Chandra* in many clusters, including A2142, A3667, RX J1720+26, and A1795. In those clusters, they are interpreted as sharp boundaries of a dense, cooler gas cloud moving with a speed v through the hotter and more rarefied ambient gas. The surface brightness edge in 2A 0335+096 appears to be a similar cold front. As discussed by Vikhlinin et al. (2001b), the pressure profile across the front can be used to determine the Mach number $M \equiv v_1/c_{s1}$ of the moving cooler gas cloud with respect to the speed of sound in the gas upstream, c_{s1}.

In Table 2, we show that the pressure jump across the front is $A_P = 1.6 \pm 0.3$. This corresponds to a Mach number for the dense central gas cloud of $M \simeq 0.75 \pm 0.2$ (see, e.g., Fig. 6 of Vikhlinin et al. 2001b). Such subsonic motion of the cool gas cores appears to be very common among the otherwise relaxed clusters with cooling flows (Markevitch, Vikhlinin, & Forman 2003a).

6.2. *X-Ray Blobs*

In the analysis above, we identified a number of X-ray blobs, most of which are likely to be part of a filamentary structure. As can been seen from Table 3, the blobs are quite dense: their densities range from ≈0.06 to 0.13 cm^{-3}. Although the projected spectral properties of the blobs are significantly different (i.e., they have different emission-weighted temperatures; see the right-hand panels of Fig. 6 and Fig. 9), in § 4.5 we show that the temperature of their immediately surrounding ambient gas and the deprojected blob temperatures are consistent within the errors for all but one of the blobs (see the top panel of Fig. 9). This is particularly interesting, as it implies that the thermal pressure of the blobs is higher than the thermal pressure of the surrounding ambient gas. This finding, however, does not necessarily mean that the blobs are out of pressure equilibrium with the ambient gas, as the latter may have extra nonthermal pressure (for example, magnetic fields and/or relativistic electrons ejected from the central active galactic nucleus [AGN]). Another possibility is that the cluster core contains some additional hot thermal gas that provides extra pressure. This gas cannot be detected in our analysis because when we estimate the ambient gas temperature, we leave the normalization of the hot background component free to vary (see § 4.5). Although with the available data we cannot exclude this possibility, it seems to be quite unlikely, as it would be difficult to heat the cluster center without any nonthermal energy input as well. Although at the moment it is not clear which physical processes may be responsible for the formation of the observed substructures, we can safely state that the system is dynamically unstable, and the presence of blobs is likely to be a transient phenomenon. We note that the evolution of the system strongly depends on the total pressure supporting the ambient gas. Below we discuss two extreme possibilities:

1. The ambient gas surrounding the blobs is only supported by thermal pressure, and thus the blobs are actually not in pressure equilibrium.
2. The ambient gas, and possibly to some extent the blobs, too, are supported by an extra nonthermal pressure component such that the blobs and the ambient gas are actually in pressure equilibrium.

In the first case, the blobs are overpressured, so we expect them to expand. The expansion time is of the order of the blobs' sound crossing time:

$$t_{\rm cross} = 2r_1\sqrt{\frac{\mu}{\gamma kT}} = 1.7\times10^7\ {\rm yr}\left(\frac{r_1}{5\ {\rm kpc}}\right)\sqrt{\frac{(\mu/0.69)m_p}{(\gamma/1.66)(kT/1.3\ {\rm keV})}}\,, \quad (6)$$

where r_1 is the radius of the blob and μ, m_p, and γ are the mean particle weight, the proton mass, and the adiabatic index, respectively. Using the linear dimension of the blobs reported in Table 3, we find $t \approx (1\text{–}2)\times10^7$ yr, which appears to be very short compared with the likely cluster age. Furthermore, the blobs' cooling time is ≈10 times longer than the dynamical time (see bottom panel of Fig. 9). Thus, in this first case, in which the external gas is not supported by an extra pressure component, the blobs should expand before their excess pressure is radiated away. Consequently, we do not expect to have a significant mass deposition into a cold phase from the blobs.

Conversely, if the blobs are in both thermal and pressure equilibrium with the ambient gas, as in the second case considered above, the blobs are likely to be more stable. Nevertheless, as the blobs are heavier than the ambient gas (they have higher densities), they are expected to sink eventually

toward the minimum of the potential well. The timescale t_s needed by the blobs to reach the cluster center is obviously $t_s \geq t_{\rm ff}$,[9] where $t_{\rm ff}$ is the free-fall time. If we assume that the cluster potential well is described by an NFW profile (Navarro, Frenk, & White 1996), the free-fall time for a point mass at rest at a radius $r \ll r_s$ can be well approximated by

$$t_{\rm ff} = \sqrt{\frac{2r}{g}}\,, \tag{7}$$

where r_s is the scale radius, $g = 2\pi G\delta_c\rho_{\rm crit}$, G is Newton's constant, $\rho_{\rm crit} = 3H^2/8\pi G$ is the critical density for closure, and δ_c is the characteristic density contrast. Using the best-fit NFW parameters for our cluster and $r \approx 20$ kpc, we find

$$t_{\rm ff} \approx 10^8 h_{70}^{-1}\sqrt{\frac{r}{20\ {\rm kpc}}}\ {\rm yr}\,. \tag{8}$$

From Table 3, we see that the free-fall and the cooling times are similar; thus, the actual sinking time is much longer than the cooling time. Therefore, unlike the first case considered above, if the ambient gas is supported by an extra nonthermal pressure component such that the gas and the blobs are in pressure equilibrium, we expect the blobs to cool down before they can actually sink into the cluster center. Hence, some mass deposition into a cold phase is possible.

6.3. *Possible Dynamical Models*

We conclude this section by discussing possible dynamical models that may explain the origin of the observed complex structure in the core of 2A 0335+096. Our starting point is the evidence for the presence of a dense gas core that moves from north to south with a Mach number $M \simeq 0.75 \pm 0.2$ (see § 6.1).

We propose two models:

1. The motion of the cool core induces instabilities that penetrate inside the core and disturb the gas.
2. The central galaxy has an intermittent AGN that causes the cool gas "bubbling."

The features observed in the cluster result from the development of hydrodynamic instabilities induced by these two phenomena. Below we discuss in detail these two models. We conclude that both models are consistent with the available data and that further observations are required to discriminate between the two cases.

6.3.1. *Core Destruction by Hydrodynamic Instabilities*

We first show that small-scale structure can be the result of hydrodynamic instabilities induced by the observed motion of the core gas (revealed by the presence of the cold front). This motion may be due to a merger, as in A2142 or A3667 (Markevitch et al. 2000; Vikhlinin, Markevitch, & Murray 2001a). or to the gas sloshing, as in many other cooling flow clusters (Markevitch et al. 2001, 2003a). The precise nature of the core motion is not important.

The orientation of the front (see, e.g., Fig. 12), together with the asymmetry in the temperature distribution (see Fig. 6), suggests that the core is moving along a projected direction that goes from north to south. If the core is in fact a merging subcluster, it is clear that in projection the position of the subcluster is very close to the cluster center (see § 3.1); from the available data, however, we cannot measure the merger impact parameter. Hence, the subcluster may in fact be passing through the cluster at any distance along the line of sight from the center.

When a dense gas cloud is moving with respect to a rarefied one, the interface between the two gases is subject to hydrodynamical Rayleigh-Taylor (R-T) and Kelvin-Helmholtz (K-H) instabilities. In the following, we estimate the effect of both instabilities on the moving core, using the same approach as Vikhlinin & Markevitch (2002). We assume that the gas cloud is a sphere of radius equal to the distance of the observed front, $R \approx 56\farcs7$ (≈39.7 kpc). As the cloud moves, the external gas flows around its border. The inflowing gas slows down at the leading edge of the sphere but reaccelerates at larger angles as it is squeezed to the sides by new portion of inflowing gas. In the case of an incompressible fluid, the velocity at the surface of the sphere is purely tangential and is given by $v_{\rm fluid} = 3/2 v_\infty \sin\varphi$, where v_∞ is the velocity of the inflowing gas at infinity and φ is the angle of the considered point on the cloud with respect to its direction of motion (see, e.g., Lamb 1945). Unfortunately, there is no analytic solution for the flow of a compressible fluid around a sphere. Nevertheless, the qualitative picture is similar. As we are only interested in order-of-magnitude estimates, in the following we parameterize the actual fluid speed, introducing the parameter η so that

$$v_{\rm fluid} = \eta v_\infty \sin\varphi. \tag{9}$$

The parameter η should range between 1 (fluid velocity at the surface of the sphere equal to the inflowing gas at infinity) and 1.5 (incompressible fluid).

First, we consider the R-T instability. This instability develops only if the acceleration induced by the drag force d_g is greater than the gravitational potential acceleration near the front due to the cluster mass inside the moving cloud. If we assume hydrostatic equilibrium, then the gravitational acceleration is given by

$$g = -\frac{kT}{\mu m_p R}\left(\frac{d\log n}{d\log r} + \frac{d\log T}{d\log r}\right)\,, \tag{10}$$

where μm_p is the mean particle mass and n and T are the gas electron density and temperature profiles, respectively. In our case, this gives $g = 1.7 \times 10^{-8}$ cm s^{-2} (see §§ 3.2 and 4.4 and Fig. 4). On the other hand, the cloud acceleration due to the drag force is given by

$$g_d = 0.15\frac{n_{\rm in}}{n_{\rm out}}\frac{M^2 c_s^2}{R}\,, \tag{11}$$

where $n_{\rm in}$ and $n_{\rm out}$ are the gas electron densities inside and outside the edge, respectively, which in our case gives $g_d = 2.5 \times 10^{-9}$ cm s^{-2}. As the drag acceleration is less than the gravitational one, then the R-T instabilities should be suppressed.

Now we consider the K-H instability. This instability may develop whenever two fluids in contact have a nonzero tangential velocity. As for the R-T instability, the presence of a gravitational field may suppress the development of the

[9] Note that $t_s = t_{\rm ff}$ just in the case in which we assume both that the gas is collisionless and that the blobs have zero angular momentum.

instability. The stability condition is such that a perturbation with wavenumber less than $k = 2\pi/\lambda$ is stable if

$$g \geq \frac{Dk(v)^2}{D^2 - 1} , \quad (12)$$

where g is the gravitational acceleration at the interface between the two regions and $D \equiv n_{\rm in}/n_{\rm out}$ is the density contrast. Using equation (9) for the tangential velocity, equation (12) becomes

$$\lambda \geq 2\pi \frac{D}{D^2 - 1} \frac{\eta^2 v_\infty^2 \sin^2 \varphi}{g} \approx (400\text{–}900) \sin^2 \varphi \text{ kpc} . \quad (13)$$

Equation (13) shows that gravity suppresses instabilities only on scales larger than 400 kpc. Hence, in the absence of other stabilizing mechanisms, we expect the formation of the K-H instabilities on smaller scales.

In the case of 2A 0335+096, we see that the instabilities on scales of the order of the radius of the sphere R may develop already at $\varphi > 18°$. The condition that the instability on the gas cloud scale can develop, although necessary, is not sufficient. In fact, in order to effectively disrupt the gas of the moving gas cloud, the growth time τ of the instability must be much shorter than the dynamical time of the system (the cluster crossing time, $t_{\rm cross}$). We thus require (see Vikhlinin et al. 2001a and the algebraic correction of Mazzotta et al. 2002)

$$\frac{t_{\rm cross}}{\tau} \sim 3.3 \frac{L}{\lambda} \sin \varphi \gg 1 . \quad (14)$$

If we assume that the cluster radius is $r = 1$ Mpc, at the angle $\varphi = 18°$ at which the instability starts to develop, we find that $t_{\rm cross}/\tau \approx 25$. Furthermore, at the much larger angle of $\varphi = 90°$, where the instabilities are most effective, we find $t_{\rm cross}/\tau \approx 83$. Therefore, they have sufficient time to grow to the nonlinear regime.

The effect of K-H instabilities is to turbulently mix the gas in the dense, moving, cool cloud with the more diffuse, hotter cluster gas. In particular, some less dense gas from the cluster could be deposited into the denser gas cloud and vice versa. Such a process may be responsible for the formation of the observed clumpy X-ray structure. Similarly, any preexisting cold (<30 K) gas deposited in the cluster and/or subcluster core by a cooling flow will also be mixed and redistributed on these scales. This would explain the observed Hα+[N II] emission morphology. On the other hand, these subsonic K-H instabilities will not produce any significant radio signature. Hence, in this scenario the radio properties of 2A 0335+096 (the minihalo and the X-ray holes) must be related to activity of the central galaxy.

In conclusion, the observed X-ray properties of the 2A 0335+096 core may be produced by K-H instabilities induced by the motion of the core.

6.3.2. *Gas Bubbling by the Central AGN*

The observed structure of 2A 0335+096 can also be accounted for if the central cluster galaxy hosts an AGN that undergoes intervals of strong activity followed by periods of relative quiescence (see, e.g., Binney & Tabor 1995; Soker et al. 2001). During each active period, the AGN inflates two bubbles by filling them with relativistic electrons. As observed in other clusters (e.g., Perseus: Fabian et al. 2000; Hydra A: McNamara et al. 2000; A2052: Blanton et al. 2001), this expansion creates an external shell where the gas is denser. The bubbles rise buoyantly, entrain the dense gas underneath them, and induce convection (see, e.g., Churazov et al. 2001). These bubbles are also subjected to hydrodynamic instabilities that destroy them, fragmenting the denser shell into what we observe as denser X-ray blobs. The observed structure in the core may be created by numerous bursts of AGN activity during which the jets point in different directions. We can visualize this process as gas bubbling induced by the energy injection from a central AGN. The difference from other clusters with similar X-ray cavities, but lacking such filamentary or blobby structure, might be caused by a shorter duty cycle of the central AGN in 2A 0335+096, on the order of 10^7 yr (see § 6.2).

After the bubble is broken by the hydrodynamical instabilities, the relativistic electrons produced by the AGN that are likely to be present inside it (see, e.g., McNamara 2002 and references therein) should eventually distribute in the central cluster region. However, they may avoid the densest gas blobs because of, for example, an enhanced magnetic field created during the shell compression induced by the bubble expansion. These electrons would add a nonthermal pressure component in the ambient (interblob) gas that may account for the apparent pressure nonequilibrium of the cluster core.

As discussed in § 6.2, in this case the dense X-ray blobs have time to cool, depositing some mass in a cold phase. This cool gas may explain the presence of the observed CO and Hα+[N II] extended emission in the cluster center (see Fig. 11). The relativistic electrons produced by the AGN may also account for the presence of the mini–radio halo observed in the cluster core (see Fig. 12).

We finally mention that there may be a connection between the AGN activity and the core sloshing, hinted at by the observed correlation between the presence of the X-ray bubbles and cold fronts in the central regions of many cooling flow clusters (Markevitch et al. 2003a). Reynolds, Heinz, & Begelman (2002) showed that during AGN jet formation, a spherical pulse forms and propagates at the sound speed into the intracluster medium. Repeated AGN activity may inject sufficient kinetic energy to produce sloshing of the gas, although it is unclear how the bulk motion of the core as a whole could be produced. Sloshing of the dense core may also be induced by a merger, even if the merging subcluster did not reach the center of the main cluster (see, e.g., Churazov et al. 2003).

To conclude this section, gas bubbling induced by central AGN provides a plausible explanation of the observed features in the cluster core.

7. CONCLUSION

The poor cluster 2A 0335+096 has several remarkable features that are only detectable with the superb resolution of *Chandra*. First, there is a cold front, indicating a mildly subsonic gas motion. Second, there are two X-ray cavities that may be associated with steep-spectrum radio emission, indicating previous radio activity in this system. Third, there are a number of small, dense gas blobs in the cluster core that may be the shred of a cooling core disturbed by either K-H instabilities or "bubbling" induced by intermittent AGN activity. All of these properties relate to processes that

may act to disrupt or destroy any cooling flow (subcluster merger, injection of nonthermal electrons into the intracluster medium, or direct radiation from an AGN). From this relatively short X-ray observation, it is not possible to determine which process (if any) dominates. Future deeper observations in the X-ray, radio, and optical of 2A 0335+096 may allow the energetics of each to be assessed. When combined with observations of other similar clusters, it will be possible to draw concrete conclusions about the astrophysical nature of cooling flows.

We thank an anonymous referee for a careful reading of the paper and for useful suggestions. We thank David Gilbank for useful comments and suggestions and for assistance with the narrowband optical image, Daniel Harris and Craig Sarazin for providing the VLA images, and Alexey Vikhlinin for helpful discussions. This work was supported by an RTN fellowship, CXC grants GO2-3177X and GO2-3164X, the Royal Society, and the Smithsonian Institution.

REFERENCES

Allen, S. W., Ettori, S., & Fabian, A. C. 2001, MNRAS, 324, 877
Allen, S. W., Fabian, A. C., Edge, A. C., Böhringer, H., & White, D. A. 1995, MNRAS, 275, 741
Anders, E., & Grevesse, N. 1989, Geochim. Cosmochim. Acta, 53, 197
Arnaud, K. A. 1996, in ASP Conf. Ser. 101, Astronomical Data Analysis Software and Systems V, ed. G. Jacoby & J. Barnes (San Francisco: ASP), 17
Bayer-Kim, C. M., Crawford, C. S., Allen, S. W., Edge, A. C., & Fabian, A. C. 2002, MNRAS, 337, 938
Binney, J., & Tabor, G. 1995, MNRAS, 276, 663
Blanton, E. L., Sarazin, C. L., & McNamara, B. R. 2003, ApJ, 585, 227
Blanton, E. L., Sarazin, C. L., McNamara, B. R., & Wise, M. W. 2001, ApJ, 558, L15
Buote, D. A. 2000, ApJ, 539, 172
Cash, W. 1979, ApJ, 228, 939
Cavaliere, A., & Fusco-Femiano, R. 1976, A&A, 49, 137
Churazov, E., Brüggen, M., Kaiser, C. R., Böhringer, H., & Forman, W. 2001, ApJ, 554, 261
Churazov, E., Forman, W., Jones, C., & Böhringer, H. 2003, ApJ, 590, 225
Cooke, B. A., et al. 1978, MNRAS, 182, 489
David, L. P., Nulsen, P. E. J., McNamara, B. R., Forman, W., Jones, C., Ponman, T., Robertson, B., & Wise, M. 2001, ApJ, 557, 546
Dickey, J. M., & Lockman, F. J. 1990, ARA&A, 28, 215
Edge, A. C. 2001, MNRAS, 328, 762
Edge, A. C., Stewart, G. C., Fabian, A. C., & Arnaud, K. A. 1990, MNRAS, 245, 559
Fabian, A. C. 1994, ARA&A, 32, 277
Fabian, A. C., Sanders, J. S., Ettori, S., Taylor, G. B., Allen, S. W., Crawford, C. S., Iwasawa, K., & Johnstone, R. M. 2001, MNRAS, 321, L33
Fabian, A. C., et al. 2000, MNRAS, 318, L65
Forman, W., Jones, C., Markevitch, M., Vikhlinin, A., & Churazov, E. 2002, in Merging Processes in Galaxy Clusters, ed. L. Feretti, I. M. Gioia, & G. Giovanni (Dordrecht: Kluwer), 109
Huchra, J. P., Wyatt, W. F., & Davis, M. 1982, AJ, 87, 1628
Irwin, J. A., & Sarazin, C. L. 1995, ApJ, 455, 497
Johnstone, R. M., Allen, S. W., Fabian, A. C., & Sanders, J. S. 2002, MNRAS, 336, 299
Kaastra, J. S. 1992, An X-Ray Spectral Code for Optically Thin Plasmas (Internal SRON-Leiden Rep., updated ver. 2.0; Leiden: SRON)
Kaastra, J. S., Ferrigno, C., Tamura, T., Paerels, F. B. S., Peterson, J. R., & Mittaz, J. P. D. 2001, A&A, 365, L99
Kikuchi, K., Furusho, T., Ezawa, H., Yamasaki, N. Y., Ohashi, T., Fukazawa, Y., & Ikebe, Y. 1999, PASJ, 51, 301
Lamb, H. 1945, Hydrodynamics (New York: Dover)
Liedahl, D. A., Osterheld, A. L., & Goldstein, W. H. 1995, ApJ, 438, L115
Markevitch, M., Vikhlinin, A., & Forman, W. R. 2003a, in ASP Conf. Ser. 301, Matter and Energy in Clusters of Galaxies, ed. S. Bowyer & C.-Y. Huang (San Francisco: ASP), in press (astro-ph/0208208)
Markevitch, M., Vikhlinin, A., & Mazzotta, P. 2001, ApJ, 562, L153
Markevitch, M., et al. 2000, ApJ, 541, 542
———. 2003b, ApJ, 583, 70
Mazzotta, P., Fusco-Femiano, R., & Vikhlinin, A. 2002, ApJ, 569, L31
Mazzotta, P., Markevitch, M., Vikhlinin, A., Forman, W. R., David, L. P., & Van Speybroeck, L. 2001, ApJ, 555, 205
McNamara, B. R. 2002, in ASP Conf. Ser. 262, The High Energy Universe at Sharp Focus: *Chandra* Science, ed. E. M. Schlegel & S. D. Vrtilek (San Francisco: ASP), 351
McNamara, B. R., Bregman, J. N., & O'Connell, R. W. 1990, ApJ, 360, 20
McNamara, B. R., et al. 2000, ApJ, 534, L135
Molendi, S., & Gastaldello, F. 2001, A&A, 375, L14
Molendi, S., & Pizzolato, F. 2001, ApJ, 560, 194
Morris, R. G., & Fabian, A. C. 2003, MNRAS, 338, 824
Navarro, J. F., Frenk, C. S., & White, S. D. M. 1996, ApJ, 462, 563
Paturel, G., Fouqué, P., Bottinelli, L., & Gouguenheim, L. 1989, A&AS, 80, 299
Peterson, J. R., et al. 2001, A&A, 365, L104
Reynolds, C. S., Heinz, S., & Begelman, M. C. 2002, MNRAS, 332, 271
Romanishin, W., & Hintzen, P. 1988, ApJ, 324, L17
Sanders, J. S., & Fabian, A. C. 2002, MNRAS, 331, 273
Sarazin, C. L., Baum, S. A., & O'Dea, C. P. 1995, ApJ, 451, 125
Sarazin, C. L., O'Connell, R. W., & McNamara, B. R. 1992, ApJ, 397, L31
Schmidt, R. W., Fabian, A. C., & Sanders, J. S. 2002, MNRAS, 337, 71
Schwartz, D. A., Schwarz, J., & Tucker, W. 1980, ApJ, 238, L59
Singh, K. P., Westergaard, N. J., & Schnopper, H. W. 1986, ApJ, 308, L51
———. 1988, ApJ, 331, 672
Soker, N., White, R. E., III, David, L. P., & McNamara, B. R. 2001, ApJ, 549, 832
Tamura, T., et al. 2001, A&A, 365, L87
Taylor, G. B., Fabian, A. C., & Allen, S. W. 2002, MNRAS, 334, 769
Vikhlinin, A., Forman, W., & Jones, C. 1999, ApJ, 525, 47
Vikhlinin, A., Markevitch, M., & Murray, S. S. 2001a, ApJ, 549, L47
———. 2001b, ApJ, 551, 160
Vikhlinin, A. A., & Markevitch, M. L. 2002, Astron. Lett., 28, 495
Voigt, L. M., Schmidt, R. W., Fabian, A. C., Allen, S. W., & Johnstone, R. M. 2002, MNRAS, 335, L7
White, D. A., Fabian, A. C., Johnstone, R. M., Mushotzky, R. F., & Arnaud, K. A. 1991, MNRAS, 252, 72
Wilms, J., Allen, A., & McCray, R. 2000, ApJ, 542, 914
Young, A. J., Wilson, A. S., & Mundell, C. G. 2002, ApJ, 579, 560